JOURNAL OF MATERIALS SCIENCE: MATERIALS IN MEDICINE **8** (1997) 559–570

Mechanical properties of carbonated apatite bone mineral substitute: strength, fracture and fatigue behaviour

E. F. MORGAN, D. N. YETKINLER*, B. R. CONSTANTZ*, R. H. DAUSKARDT
Department of Materials Science and Engineering, Stanford University, Stanford, CA 94305-2205, USA
**Norian Corporation, 10260 Bubb Road, Cupertino, CA 95014-4166, USA*

The synthesis and properties of carbonated apatite materials have received considerable attention due to their importance for medical and dental applications. Such apatites closely resemble the mineral phase of bone, exhibiting superior osteoconductive and osteogenic properties. When formed at physiological temperature they present significant potential for bone repair and fracture fixation. The present study investigates the mechanical properties of a carbonated apatite cancellous bone cement. Flexural strength was measured in three and four point bending, and the fracture toughness and fatigue crack-growth behaviour was measured using chevron and disc-shaped compact tension specimens. The average flexural strength was found to be ~ 0.468 MPa, and the fracture toughness was $\sim 0.14\ \mathrm{MPa}\sqrt{\mathrm{m}}$. Fatigue crack-growth rates exhibited a power law dependence on the applied stress intensity range with a crack growth exponent $m = 17$. The fatigue threshold value was found to be $\sim 0.085\ \mathrm{MPa}\sqrt{\mathrm{m}}$. The mechanical properties exhibited by the carbonated apatite were found to be similar to those of other brittle cellular foams. Toughness values and fatigue crack-growth thresholds were compared to other brittle foams, bone and ceramic materials. Implications for structural integrity and longer term reliability are discussed.

---

1. Introduction

The synthesis and properties of apatitic materials which closely resemble the mineral phase of bone have received considerable attention due to their importance for medical and dental applications [1]. For example, hydroxyapatite (HA) and tricalcium phosphate mixtures have been used extensively as sintered coatings to promote bone ingrowth on load-bearing prosthetic components. In addition, such porous coatings provide mechanical interdigitation and encourage bone ingrowth without the formation of intervening fibrous tissue [2, 3]. More recently, however, attention has been focused on carbonated apatites in which carbonate ions (CO_3^{-2}) substitute in either phosphate (PO_4^{-3}) or hydroxyl (OH^{-1}) sites to form a bioactive apatite with enhanced dissolution and osteoclast mediated resorption properties [4]. In particular, such carbonated apatites formed from a cementitious paste at physiological temperatures hold the promise of *in vivo* fixation of fracture sites. Applications include repair of distal radius and tibial plateau fractures and augmentation of the sliding hip-screw in femoral intertrochanteric fractures.

The superior osteogenic properties of carbonated apatites formed at low temperature from a cementitious reaction can be explained by the microstructural and chemical similarities of such apatites to bone mineral [5, 6]. Preliminary investigations of routine bone remodelling mechanisms have clearly identified Haversian canals tunnelling through a commercially produced carbonated apatite within several weeks of implantation (Fig. 1) [7]. X-ray diffraction results show that, like the mineral phase in bone, carbonated apatites have a low crystalline order and small crystal size as compared to pure mineral hydroxyapatite [4, 8]. The crystalline imperfections and distorted crystal structure in bone mineral and carbonated apatite are largely due to the substitution of carbonate anions in phosphate sites [9, 10]. These characteristics also contribute to the higher solubility of bone mineral and carbonated apatite as compared to sintered hydroxyapatite. In addition, similar calcium-to-phosphate ratios and Scherrer perfect crystal size of bone and the carbonated apatite under investigation are also apparent; typical values are presented for comparison in Table I.

Studies investigating the mechanical properties of apatites show that microstructural and mechanical characteristics strongly depend on preparation conditions, including the temperature, pressure during formation, and, for apatites formed from aqueous solutions, the liquid-to-solids ratio [12]. In general, sintered hydroxyapatites show the highest strength values [13], yet the high temperatures involved in their formulation limit their biomedical applications. Apatites that can be shaped and moulded *in vivo*

0957–4530 © *1997 Chapman & Hall*

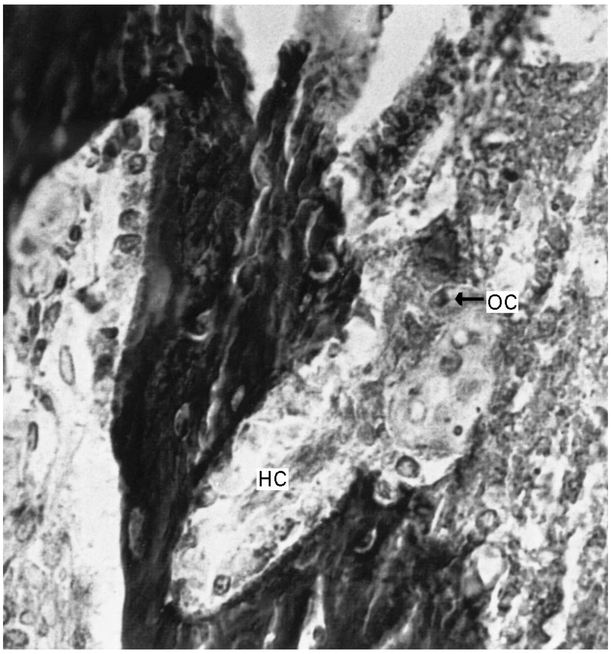

Figure 1 Optical histologic micrograph indicating evidence of osteoclastic remodelling of carbonated apatite material. Both Haversian canals (HC) and associated osteoclat (OC) are clearly seen extending from the host bone (light grey) into the calcium phosphate material (dark grey) [7].

TABLE I Comparison of bone mineral and carbonated apatite [4, 8, 11]

	Bone	Carbonate apatite
Ca/P	1.66–1.77	1.67
% CO_3 (by weight)	4.65	4.6
Scherrer crystal size (nm)	~ 20	~ 20

before hardening at physiological temperature present the greatest possibilities for bone repair although currently at a significant strength penalty. For example, Martin and Brown [12] compared the mechanical properties of calcium-deficient and carbonated hydroyapatites formed at physiological temperature. Specimens prepared at a pressure of 70 MPa had compressive strengths of 142 MPa for the calcium-deficient and 67 MPa for a carbonated apatite. Flexural strengths in three-point bending were 14 MPa and 12 MPa, respectively. The above compressive and tensile strengths are typically 60–85% lower than similarly obtained values reported for both dense and porous *sintered* hydroxyapatites [14].

Typical of brittle ceramic materials in which fracture strength is flaw dominated, the strength of carbonated apatites is found to be strongly dependent on internal porosity. Logarithmic increases in strength have been reported with decreasing porosity obtained by changing the liquid-to-solids ratio of wet reactants for carbonated apatites produced at physiological temperatures [12]. Similar increases in the fracture toughness (K_{Ic}) have been reported with decreasing porosity for sintered hydroxyapatite [15]. However, fracture toughness data is not currently available for carbonated apatites formed through cementitious reactions at physiological temperatures. There is a similar paucity of data for the extension of flaws or cracks due to subcritical crack-growth processes, for example, from cyclic fatigue crack growth. Accordingly, the intent of the present study was to investigate the mechanical properties of a commercially available carbonated apatite bone mineral substitute formed at physiological temperature. Specifically, the flexure strength was measured in both three and four-point bending to account for brittle fracture statistics. In addition, the fracture toughness and fatigue crack-growth behaviour were measured using techniques specially adapted for testing of extremely brittle materials. Data are compared to other brittle materials and fracture mechanisms discussed in terms of the prevailing microstructure and inelastic deformation characteristics.

2. Experimental techniques

2.1. Material preparation

The carbonated apatite selected for study was a bone mineral substitute known as Norian Skeletal Repair System, SRS® (Norian Corporation, Cupertino, CA).

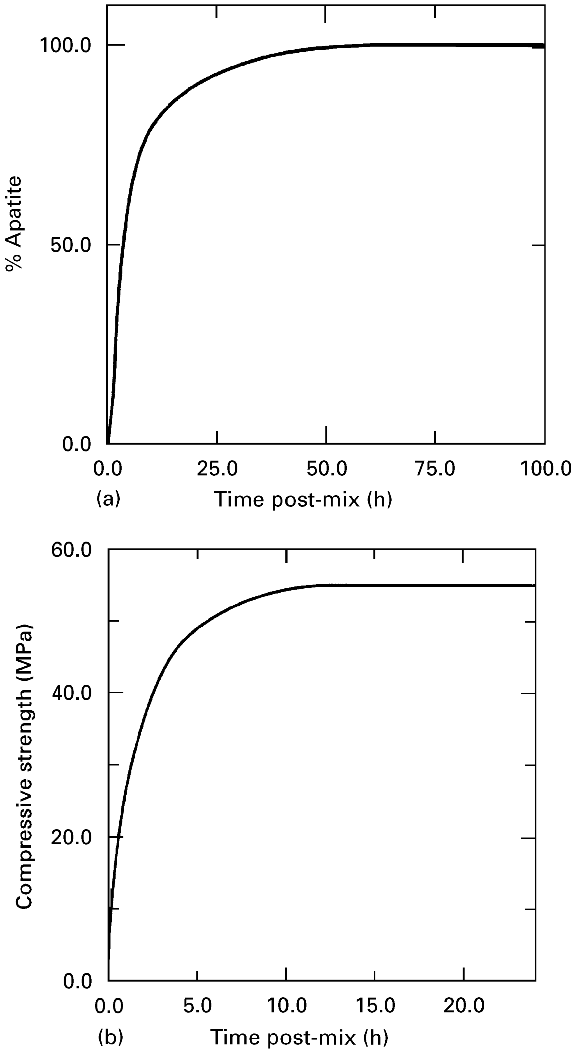

Figure 2 Mineralogic development of carbonated apatite material indicating (a) the percentage of carbonated apatite formed, and (b) the compressive strength development during curing in bovine serum at 37 °C [16].

Norian SRS was supplied as a three-component system: a calcium source powder containing tricalcium phosphate and calcium carbonate, a phosphate source powder containing monocalcium phosphate monohydrate, and a phosphate-buffered solution. Preparation of Norian SRS consists of a dry mix, a wet mix, a setting time, and a curing period. The 30 s dry mix involves mixing the two source powders together with a mortar and pestle. The solution is then added and a 2 min wet mix ensues. After mixing, the Norian SRS has a paste-like consistency and is injectable into the fracture site or sample mould during a working period of ~ 5 min. Reaction rate is temperature dependent and subsequent hardening of the paste over the following 20 min is accelerated at physiological temperature of 37 °C. The curing process takes place over the following 20–40 h (Fig. 2a), although after 1 h SRS has achieved 50% of its ultimate compressive strength of 55 MPa (Fig. 2b).

The formation of the present carbonated apatite is a cementitious reaction which hardens via an acid/base neutralization reaction. The reaction begins on the surface of the reactant calcium and phosphate source particles once wetting has occurred. A solution/reprecipitation mechanism results in the formation of an intermediate dicalcium phosphate dihydrate (brushite) phase. As the reaction product encases the reactants, the reaction grows inward, decreasing the size of the reactant cores. Bridges are also formed between the encased reactant particles leading to microporosity between the particles (< 1 μm in size). The bridging structure becomes more dense over time, decreasing the porosity to $\sim 50\%$ and leading to a final carbonated apatite with a molar calcium-to-phosphate ratio of 1.67 [8]. The microstructural development of calcium phosphate during curing has been documented [16] and is reproduced in Fig. 3 which shows a sequence of SEM micrographs taken at various times after mixing. Similar to the mineral phase of bone, the final carbonated apatite has a cellular microstructure which behaves, from a mechanical property viewpoint, like a brittle cellular foam. This resemblance is considered throughout the remainder of the study.

2.2. Flexural strength and hardness

Tensile flexural strength measurements were performed in both three- and four-point bending on rectangular bars 10 × 10 mm in cross-section and 78 mm long. The flexure bars were prepared by packing wet SRS paste into a Delrin mould. The mould was placed on a vibrating platform for 30 s which caused SRS to flow, evenly filling the mould and substantially reducing the macroporosity compared to samples prepared with no vibration. A mould cover was subsequently clamped in place to apply a pressure during the setting phase of ~ 10 MPa. The mould was immediately placed in a water bath at 37 °C for 20 min. The specimen was then removed from the mould and placed in

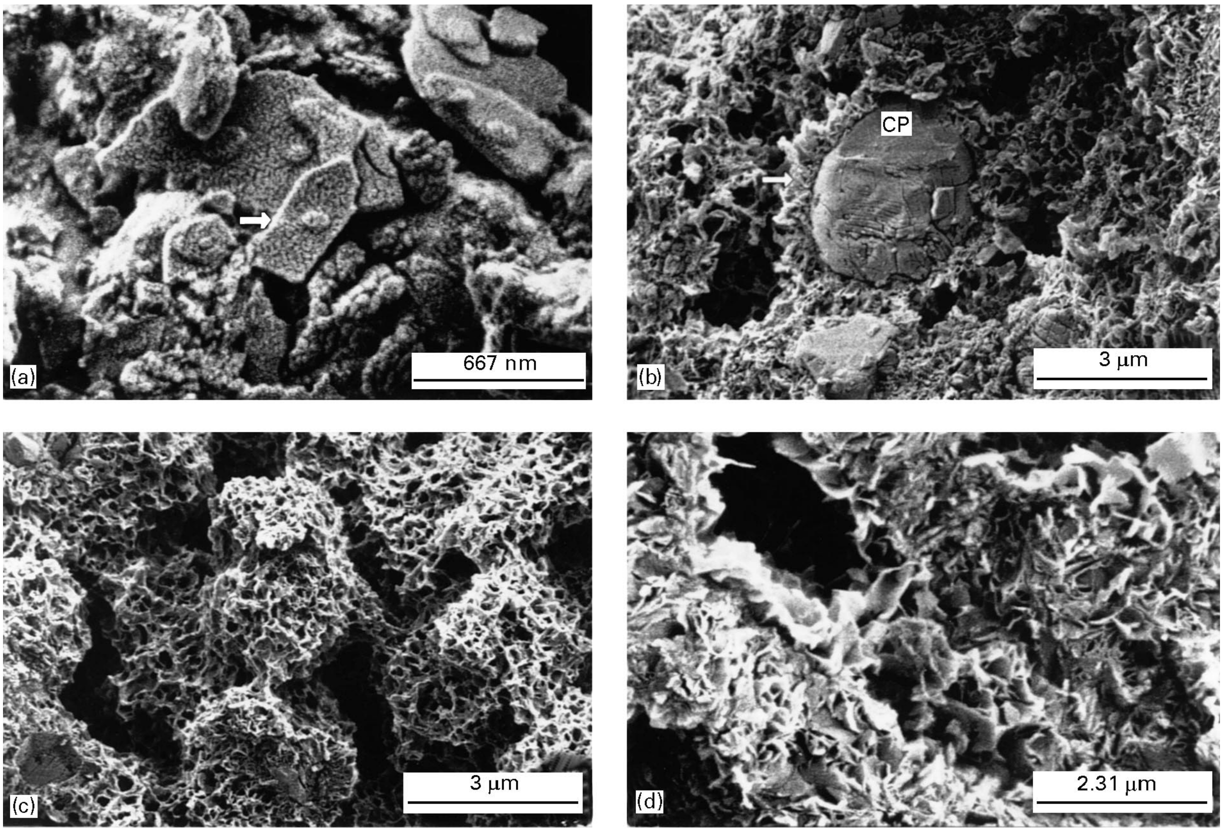

Figure 3 Microstructural development of a carbonated apatite material during curing showing (a) thin plates of brushite among reactant particles immediately after mixing, (b) a tricalcium phosphate reactant particle surrounded by brushite after 12 minutes, (c) the honeycomb structure of the carbonated apatite after 1 hour, and (d) the final morphology similar to a brittle cellular foam with small crystals of carbonated apatite forming the cell walls [16].

a phosphate-buffered Ringer's solution at 37 °C where it was allowed to cure for 24 h. All four long sides of the specimens were wet-sanded with 600- and 1000-grit sandpaper and the corners of the cross-section given slight radii to reduce the occurrence of sample failure at corner flaws during testing. The specimens were continually immersed in the phosphate-buffered solution until testing in order to simulate *in vivo* conditions.

The flexure bars were subsequently tested in three- and four-point bending using an outer loading span of 52 mm and for the four-point bend an inner span of 26 mm in a fully articulating bend fixture. Particular care was taken to ensure that the loading rollers were properly aligned on the sample surface to prevent off-axial loads. Testing was conducted in an electro-servo-hydraulic mechanical test system (MTS-810 load frame with MTS-458 analog controller) with a displacement rate of 0.5 μm/s. Flexure bar displacements, measured with a high resolution displacement transducer attached close to the sample load points, was recorded as a function of the applied loads on an X–Y recorder. Appropriate corrections were made for eccentric load application, contact point tangency shift, and changes in moment of inertia of the cross section due to the round corners [17].

Polished surfaces of the fractured bend samples were subsequently used for hardness measurements using a Vicker's diamond indenter. Since the hardness of a brittle foam is known to be a strong function of the indenter contact area, hardness values of the carbonated apatite material were measured as a function of the indenter contact area which was varied by using indentation loads in the range 0.2–1.5 kg. Reported hardness values were obtained by averaging data from at least 10 indentation impressions.

2.3. Fracture toughness

Fracture toughness of the calcium phosphate material was measured using two fracture mechanics based techniques specially developed for brittle materials testing: chevron-notched bars without a starter crack, and disc-shaped compact tension specimens containing long (> 5 mm) through thickness fatigue precracks. The chevron-notched bar fracture toughness method has the advantage of not requiring precracking of the sample to produce an atomically sharp crack and has been used extensively for brittle materials testing where precracking is extremely difficult [see 18–20]. Instead, stable crack growth is assumed to occur in the increasing thickness of the chevron region until at maximum applied load, unstable fracture occurs. The crack length at unstable fracture is not required to determine K_{Ic}. Alternatively, more accurate measures of the toughness can be obtained using compact-tension samples containing controlled, atomically sharp precracks. These techniques have been specially adapted for brittle materials testing [21] and used for fracture toughness and subcritical crack-growth measurements in very low toughness pyrolytic carbon materials used for prosthetic heart valve applications [22, 23]. This method, however, involves significantly more complex experimental precracking, crack length monitoring and mechanical testing capabilities. Both specimen types were machined wet and kept immersed in 37 °C phosphate-buffered Ringer's solution until testing.

2.3.1. Chevron-notched bar test

Flexure bars for the chevron-notch test were prepared in the same manner and of the same size as for strength testing. The chevron notch was carefully machined using a 300 μm thick circular diamond saw blade. The cross-sectional dimensions of the chevron-notch region are shown in Fig. 4a. Samples were loaded in a fully articulating four-point bend fixture with inner and outer loading spans of 20 and 40 mm, respectively. Loading was accomplished in similar fashion to the strength tests and applied loads recorded as a function of the load point displacement. Further details of the method have been described elsewhere [18].

The fracture toughness, K_{Ic}, was calculated using the equation derived by Munz *et al.* [18]:

$$K_{\mathrm{Ic}} = \frac{P}{B\sqrt{W}} Y^*_{\min} \tag{1}$$

where P is the applied load at failure, B the sample thickness, and W the width. Y^* is a dimensionless

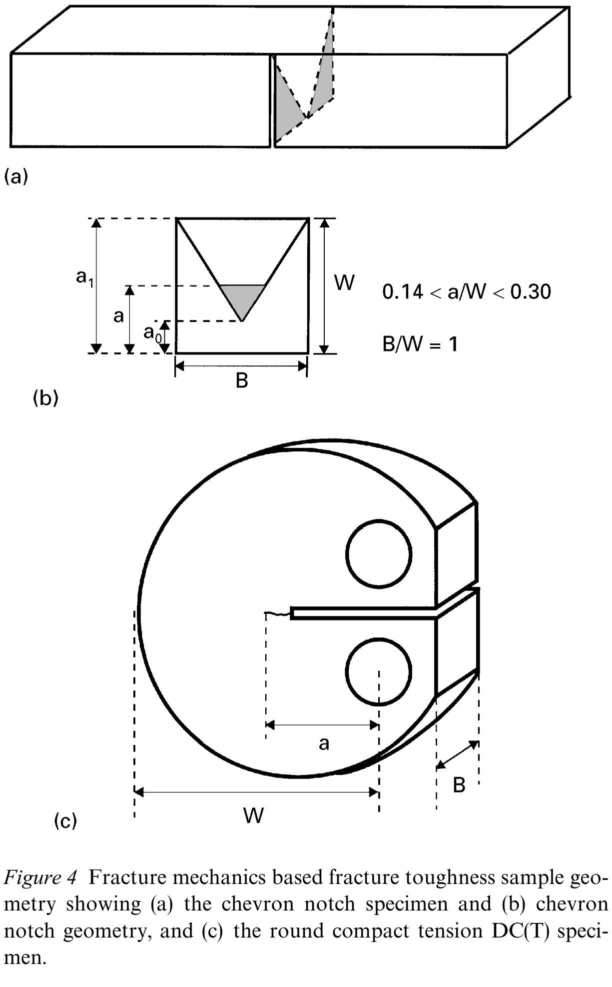

Figure 4 Fracture mechanics based fracture toughness sample geometry showing (a) the chevron notch specimen and (b) chevron notch geometry, and (c) the round compact tension DC(T) specimen.

coefficient dependent on specimen geometry and is given by:

$$Y^{*}_{\min} = (3.08 + 5.00\alpha_0 + 8.33\alpha_0)\left(\frac{S_1 - S_2}{W}\right) \times \left(1 + 0.007\left(\frac{S_1 \cdot S_2}{W^2}\right)^2\right)\left(\frac{\alpha_1 - \alpha_0}{1 - \alpha_0}\right) \quad (2)$$

where S_1 and S_2 are the inner and outer loading spans, respectively, and α_0, α_1 ($\alpha_i = a_i/W$) and W are dimensions shown in Fig. 4b.

2.3.2. Compact-tension test

Disc-shaped compact-tension specimens DC(T) were machined from 51 mm round blanks prepared in a Delrin mould using identical procedures to those described for the strength samples. Machining was performed after a 5-day curing period to allow the samples to achieve maximum strength, thereby reducing inadvertent sample breakage. The resulting DC(T) samples had standard in-plane dimensions scaled according to the specifications of ASTM E399–90 for the *Plane-Strain Fracture Toughness of Metallic Materials* [24] with a width $W = 39$ mm and a thickness $B = 6$ mm (Fig. 4c). One side of each specimen was polished to an optical finish to permit *in situ* observation of the crack during testing. Fracture toughness was determined under monotonically increasing loads (displacement control) following precracking and cyclic fatigue crack-growth testing described below. Procedures essentially conform to ASTM E399–90 for the measurement of toughness at incipient crack extension [24]. Since these tests all involve sharp cracks, measured toughness values may be smaller than values obtained from techniques that rely on a machined blunt notch as the initial crack. Such discrepancies have previously been reported for pyrolytic carbon/graphite composites [22]. Testing was conducted in an environmental chamber surrounding the sample which contained de-ionized water.

The fracture toughness, K_{Ic}, was calculated using standard handbook solutions for the applied stress intensity factor in terms of the applied load P and crack length a as [25]:

$$K_{\mathrm{Ic}} = \frac{P}{B\sqrt{W}} f(a/W) \quad (3)$$

where

$$f(a/W) = \frac{(2 + a/W)(0.76 + 4.8a/W - 11.58(a/W)^2 + 11.43(a/W)^3 - 4.08(a/W)^4)}{(1 - a/W)^{3/2}} \quad (4)$$

Owing to the extreme brittleness of the present carbonated apatite material, the initiation of the precrack was one of the most critical procedures in the test. A preliminary value for the fracture toughness, K_Q, was measured by loading one specimen without pre-cracking to failure. Such values have been previously used to estimate the toughness of diamond [26]; an approximate analysis to allow for the deviation of the notch root radius (76 μm) from the sharp crack assumption indicates that the value of K_{Ic} may be 50% less than K_Q. In the current work, the measured value of $K_Q = 0.1$ MPa$\sqrt{\mathrm{m}}$ was used to determine a suitable $\Delta K (= K_{\max} - K_{\min})$ value for fatigue pre-cracking. (Subsequent comparison of the value of K_Q with K_{Ic} values measured using sharp precracks indicated that $K_Q \sim K_{\mathrm{Ic}}$ presumably because the extreme brittleness of the material resulted in precracks emanating from the machined notch.) Stable crack initiation was facilitated by machining a wedge-shaped starter notch and by carefully growing the crack roughly 5 mm out of this region by fatigue under computer control. Crack initiation was detected by carefully monitoring the load point displacements and sample compliance during initial cyclic loading.

2.4. Fatigue-crack growth

Cyclic fatigue-crack propagation was measured prior to fracture toughness testing using the DC(T) specimens described above in general accordance with the ASTM Standard E 647-86a for measurement of fatigue-crack growth rates in metallic materials [27]. These standard techniques have been modified for brittle materials using procedures outlined by Dauskardt and Ritchie [21, 22]. Specimens were cyclically loaded at a load ratio $R(= K_{\min}/K_{\max}$, where $K_{\min}$ and $K_{\max}$ are the minimum and maximum values of the applied waveform, respectively) of 0.1 and a frequency of 25 Hz (sine wave) in closed-loop stress-intensity control. Testing was performed in an environmental chamber surrounding the sample with de-ionized water. The chamber was equipped with a viewing port to facilitate direct optical observation of the crack.

Crack length was continually measured both optically and using compliance techniques. Optical measurements were achieved using an optical microscope with a long focal distance on a high resolution translation stage to a resolution of ~20 μm. Using a high resolution displacement sensor, the load point displacement was monitored as a function of the applied loads to determine the specimen compliance. Crack length was then determined using standard numerical compliance techniques to a resolution of ~50 μm. Compliance measurements were also corrected for any nonlinear behaviour at lower loads associated with fatigue crack closure effects rising from premature contact of the fracture surfaces during the unloading cycle [28].

Due to the extreme brittleness of the material, crack-growth rates, $\mathrm{d}a/\mathrm{d}N$, were only determined under computer-controlled K-decreasing conditions over the range $\sim 10^{-6}$ to 10^{-9} m/cycle. The crack-growth fatigue threshold, ΔK_{TH}, is generally defined operationally as the maximum value of ΔK at which growth rates do not exceed 10^{-10} m/cycle, consistent with ASTM E 647 procedures [27]. In the present experiments, thresholds were approached by varying the applied loads so that the instantaneous values of crack length (a) and ΔK changed according to the equation [29]:

$$\Delta K = \Delta K_0 \exp[C^*(a - a_0)] \tag{5}$$

where a_0 and ΔK_0 are the initial values of a and ΔK, and C^* is the normalized K-gradient $((1/K)(\mathrm{d}K/\mathrm{d}a))$, which was set to $\pm\, 0.08\ \mathrm{mm}^{-1}$. Data are presented in terms of the applied stress-intensity range ($\Delta K = K_{\max} - K_{\min}$). Stress intensities were computed from Equation 3.

3. Results and discussion

3.1. Flexural strength and hardness

Load versus displacement curves measured during flexure testing of three- and four-point bend bars were essentially linear until failure, indicating that very little inelastic deformation had occurred (Fig. 5). Only very slight nonlinearity was evident at loads in excess of 85–95% of the fracture load. Average mechanical properties are presented in Fig. 6 and summarized in Table II. (Note that the values reported should only be used as an indication of strength. In brittle materials, strength is controlled by fracture processes initiated from pre-existing distributions of flaws. Strength values should properly be interpreted using a Weibull statistical approach, however, the large number of tests required was beyond the scope of the present study.) Also included in the table for comparison are tensile and compression test results performed on samples which were allowed to set under a pressure of 10 MPa and subsequently cured for 24 h in a phosphate buffered solution at 37 °C [30]. SEM micrographs of the resulting fracture surfaces showed extensive microcracking concentrated around macropores. Failure appeared to initiate at surface flaws (pores) (Fig. 7a) and the initiation site was often surrounded by subtle beach markings. Fractures were not confined to one fracture plane indicating that multiple cracks may have formed and linked to produce the final fracture surface containing abrupt changes in fracture plane (Fig. 7b).

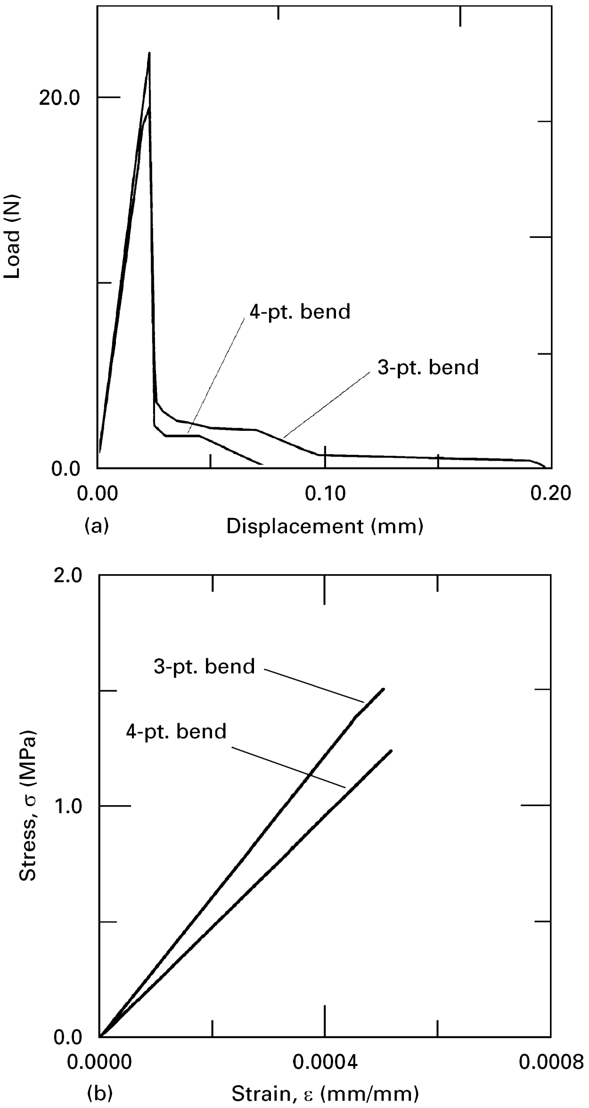

Figure 5 (a) Load versus displacement curves and (b) stress versus strain curves measured using wet three- and four-point bend samples at a displacement rate of 0.5 μm/s.

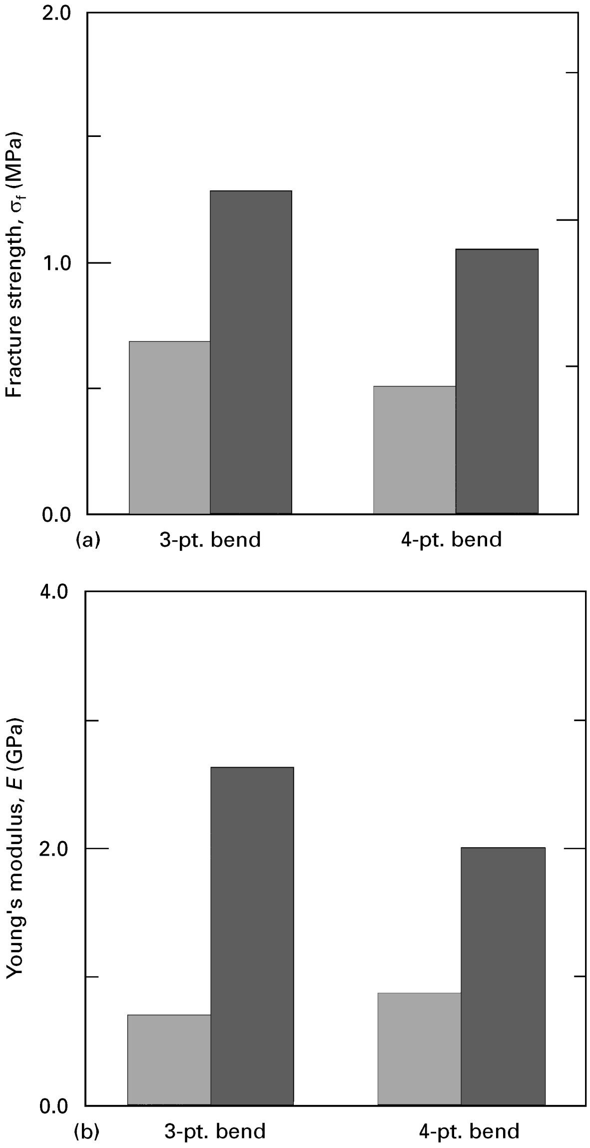

Figure 6 Average flexural strength and elastic modulus of Norian SRS carbonated apatite material determined using three- and four-point end samples tested immediately after removal from (▨) phosphate-buffered Ringer's solution (wet) and (■) after exposure to ambient laboratory air for 15 min (dry).

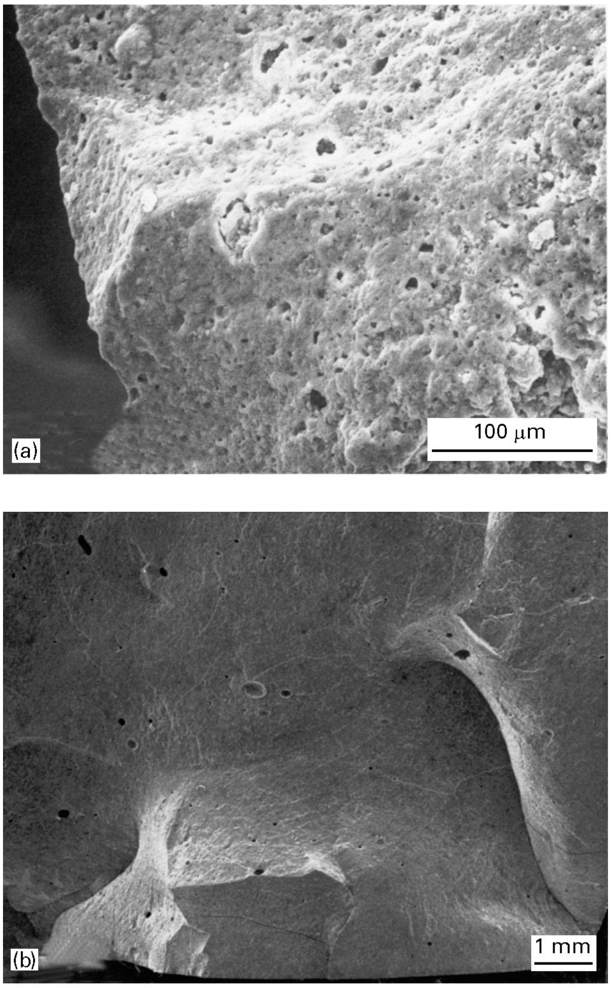

Figure 7 SEM micrographs of representative fracture surfaces obtained during strength testing, showing (a) fracture initiation typically associated with large surface pores, and (b) evidence that multiple initiation sites lead to resulting fracture surfaces with abrupt changes in fracture plane.

Similar to bone, the carbonated apatite under investigation has a cellular structure (porosity $\sim 50\%$) which, from a mechanical property viewpoint, appears to behave like a brittle foam. In tension, the linear elastic behaviour is controlled by cell wall bending and stretching to the yield stress, σ_{ys}, followed by inelastic hardening behaviour as the cell walls microcrack and rotate towards the tensile axis [31]. In brittle foams, plastic behaviour is often curtailed by fracture at a weak cell wall or pre-existing defect. For the present materials, the statistical nature of such premature brittle fracture is clearly revealed by the lower flexure strengths measured in four-point compared to three-point bending (Fig. 6). This is consistent with the probability of finding a larger (and hence weaker) flaw in the four-point flexure test; the constant outer fibre stress between the inner loading points of the four-point test samples has a greater surface area and therefore a greater probability of failing from a larger flaw. In compression, significantly higher strengths are apparent as higher loads are required to cause collapse of the cell walls by brittle crushing.

A significant reduction in strength was measured for samples that were allowed to dry for 15 min prior to testing. Two effects are consider to promote such strength degradation. First, water is absorbed during curing as the apatite forms in a hygroscopic reaction. Removing the samples from solution therefore results in drying as the water both evaporates and is absorbed by the apatite reaction. Differential shrinkage of the sample between the surface layers and interior results in microcracking which was apparent by inspection of the samples. When present, microcracking may clearly be expected to significantly decrease the fracture stress. A second effect which may result in increased strength in the wet samples is associated with the additional force required to cause viscous flow of the fluid through the interconnected porosity of the open cellular structure. An investigation of the contribution of viscous flow to the strength of a number of cellular solids has been undertaken; the effect was found to be dependent on the strain rate, the viscosity of the fluid and the reciprocal of the cell size, squared [31]. Clearly a strain rate dependence of the measured strengths should therefore be anticipated for carbonated apatite materials.

The hardness of brittle foams is known to be dependent on the indenter area. This dependency results from a statistical process in which larger indenter areas sample a greater number of cell walls leading to a *maximum* indentation stress inversely proportional to $A^{1/2}$, where A is the indentation area [31]. The size effect has been shown to persist to values of A much larger than the cell size. In addition, while the smaller indentation area might produce a larger indentation stress, it also has a greater probability of not contacting as many cell walls leading to a greater scatter of hardness data. Both trends were observed in the present study. The effect of indenter load on the Vicker's hardness, H_V, of the carbonated apatite material studied is shown in Fig. 8. Decreasing hardness with increasing indenter load and hence indenter contact area is clearly apparent in the figure. Similar trends are observed if the indentation stress (indentation

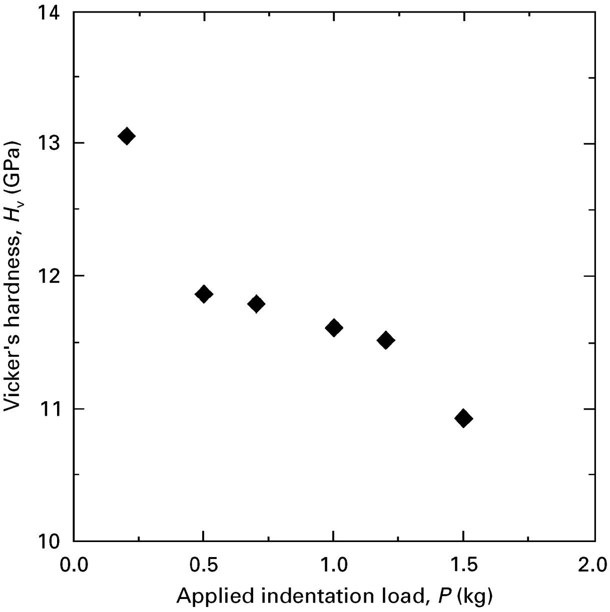

Figure 8 Vicker's hardness of Norian SRS carbonated apatite as a function of the applied indentation load, P.

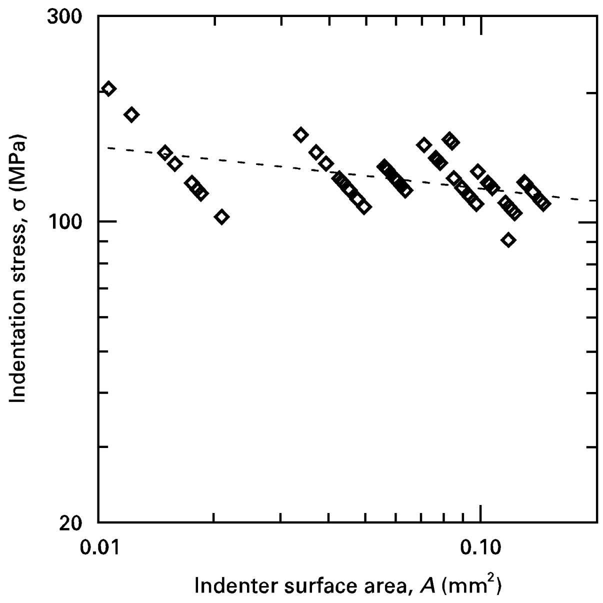

Figure 9 Indentation stress plotted as a function of the indentor contact area clearly indicates the trend of decreasing indentation stress with increasing indentor contact area expected for brittle cellular foams. Dashed line indicates average value of indentation stress data.

TABLE II Flexure strength and elastic modulus of Norian SRS™ carbonated apatite

Number of samples	Test	Environment	σ_f (MPa)	σ_{ys} (MPa)	E (GPa)
1	3-pt	dry	0.69	0.47	0.70
2	3-pt	wet	1.29	–	2.64
6	4-pt	dry	0.51	0.41	0.87
2	4-pt	wet	1.06	–	2.01
–	Tension[1]	wet	2.1	–	–
–	Compression[2]	wet	55	–	–

[1] Dimetral tension test [8, 30].

[2] Tested in accordance with ASTM F451 [30].

load/projected indenter area) is plotted as a function of the indenter contact area as shown in Fig. 9; the average value of the indentation stress is shown as a dashed line. In addition, the expected increase in scatter of the data is also clearly apparent for smaller indenter contact areas.

The effect of contact area on indentation stress may be important when carbonated apatite materials are used in fracture fixation. In these applications, the material is used as a cement between two rough substrates. Asperities on either of the adjacent substrates may result in high local stresses. This may, however, be counteracted by the increasing hardness (indentation stress) associated with smaller contact areas. These effects may have implications for attaching carbonated apatite materials to high modulus substrates such as metallic screws in bone fixation application. On the other hand, compliant substrates tend to sample a greater number of cell walls. These considerations, however, are beyond the scope of the present study.

3.2. Fracture toughness

Due to the extreme brittleness of the present material, the fracture toughness was initially assessed using the chevron notched beam technique which was specifically developed for brittle materials testing. The average fracture toughness value determined was $K_{\mathrm{Ic}} = 0.06\ \mathrm{MPa}\sqrt{\mathrm{m}}$. Following fracture, the initial crack length which occurred before unstable fracture of the sample at maximum load was determined by optical examination of the fracture surfaces. The resulting values of K_{Ic} are plotted as a function of crack length in Fig. 10. Also included in the figure are values of K_{Ic} determined using DC(T) samples discussed below. No clear trends of toughness with stable crack extension were observed for the chevron notch samples. It should be noted that the chevron notch test is not expected to produce accurate values of the toughness given complexities of crack growth in a variable thickness notched region as well as assumptions made regarding the analysis of the associated load displacement data (the analysis implicitly includes a crack length at unstable fracture). The data does, however, provide an indication of the extremely brittle nature of the SRS material.

While significantly more complex experimentally, values of the plane strain fracture toughness determined using DC(T) fracture mechanics samples are considered to be more accurate and provided an average $K_{\mathrm{Ic}} = 0.14\ \mathrm{MPa}\sqrt{\mathrm{m}}$. Individual values of K_{Ic} are plotted as a function of the fatigue pre-crack length in Fig. 10. No clear evidence of resistance-curve (R-curve) behaviour in which the resistance to crack growth increases with initial crack extension was apparent. Such behaviour is typical of many brittle materials in which toughening in a process zone surrounding the crack, or bridging elements spanning the crack faces, results in irreversible energy dissipation in the crack wake [32]. However, since toughness measurements were conducted after fatigue testing,

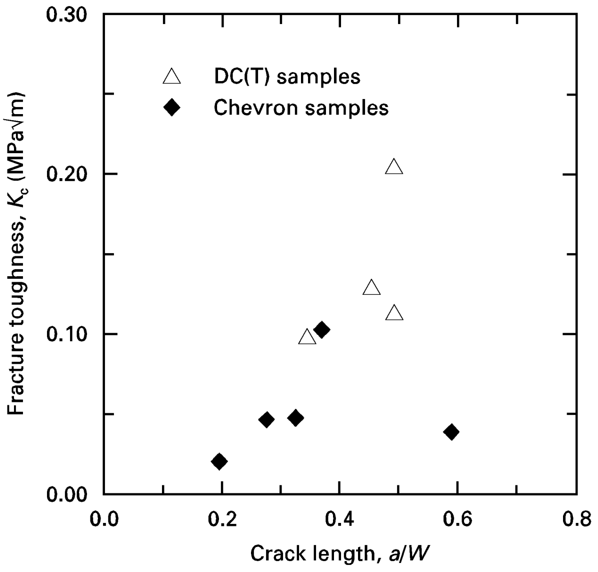

Figure 10 Fracture toughness determined using chevron-notched bend bars (◆) and ASTM-styled disc-shaped compact tension samples (△) plotted as a function of the critical crack length at fracture.

the entire R-curve may not be sampled since crack extension would begin at the final value of K_{max} of the previous fatigue loading cycle. Similar to the chevron notch tests, a relatively large scatter in the DC(T) toughness values was also apparent. Such scatter is not uncommon for low toughness brittle materials, for example, similar scatter has been reported in the R-curve toughness behaviour of pyrolythic carbon materials [22, 23].

The toughness of the present carbonated apatite material is low compared to most engineering materials, although it is similar to other brittle cellular materials such as pyrolythic carbon composites ($K_c \sim 1.6 \mathrm{MPa}\sqrt{\mathrm{m}}$) used for artificial heart valve prostheses [33], chalk ($K_c \sim 0.09$ MPa$\sqrt{\mathrm{m}}$) [29], dental enamel ($K_c \sim 1$ MPa$\sqrt{\mathrm{m}}$) [34], and many brittle polymer and ceramic foams where toughness values of ~ 0.1 MPa$\sqrt{\mathrm{m}}$ have been reported [35, 36]. These values have important implications for the resulting strength of the material, which is fracture dominated, as well as for the associated flaw tolerance and long-term reliability. Alternatively, when processed as elevated temperature, the fracture toughness of sintered hydroxyapatites has been recorded as high as 1 MPa$\sqrt{\mathrm{m}}$ when the porosity was reduced to 5% [15]. Interestingly, while the SRS carbonated apatite is similar in composition and cellular structure to the mineral phase of bone, the toughness of wet bone is considerably higher at 2–7 MPa$\sqrt{\mathrm{m}}$ [37], and generally about 60% lower when thoroughly dried. Only at very high strain rates ($\sim 7\,\mathrm{s}^{-1}$) were comparable toughness values of ~ 0.23 MPa$\sqrt{\mathrm{m}}$ reported for bone [38]. The large difference in the fracture toughness of bone and SRS can in part be attributed to the composite nature of wet bone, containing both organic and inorganic (mineral) phases. Even when dried, the organic phase containing strong collagen fibres and other organic matter imparts significant toughness to the otherwise brittle cellular structure. Interesting possibilities therefore exist for toughening carbonated apatite materials through incorporation of reinforcement phases either in the form of hard particles or platelets, or in the form of organic second phases.

3.3. Fatigue crack-growth behaviour

Cyclic fatigue-crack propagation data as a function of the applied ΔK measured in a de-ionized water environment are plotted in Fig. 11. The cyclic fatigue-crack propagation of Norian SRS displays a power-law dependence on the stress-intensity range similar to metallic materials and in agreement with data from a wide range of other brittle ceramic materials [21–23, 39]. Growth rates can be fitted to a conventional Paris law relationship [40] of the form:

$$\frac{\mathrm{d}a}{\mathrm{d}N} = C(\Delta K)^m \qquad (6)$$

where the constant C and crack-growth exponent m have values of 1.03×10^{11} and 17, respectively. These values typically depend on the material and environmental combination. The value of m (representing the slope of the fatigue growth-rate curve) is in the range commonly observed for brittle materials (e.g. 10 – 80), but is considerably larger than typically reported for metals (2–4). The value of the fatigue threshold, ΔK_{TH}, measured at a maximum growth rate of $\sim 10^{-9}$ m/cycle, was found to be ~ 0.085 MPa$\sqrt{\mathrm{m}}$ which is approximately 60% of K_{Ic}, again typical of other brittle ceramic materials. Values of C, m and ΔK_{TH} for the SRS carbonated apatite tested are compared with other ceramic and brittle cellular materials in Table III. Similar to fracture toughness values, fatigue crack-growth rates and associated fatigue threshold occur at extremely low values of the applied stress intensity range, ΔK. To the best of our knowledge, only brittle polyurethane foams exhibit fatigue crack growth at such low values of the applied ΔK.

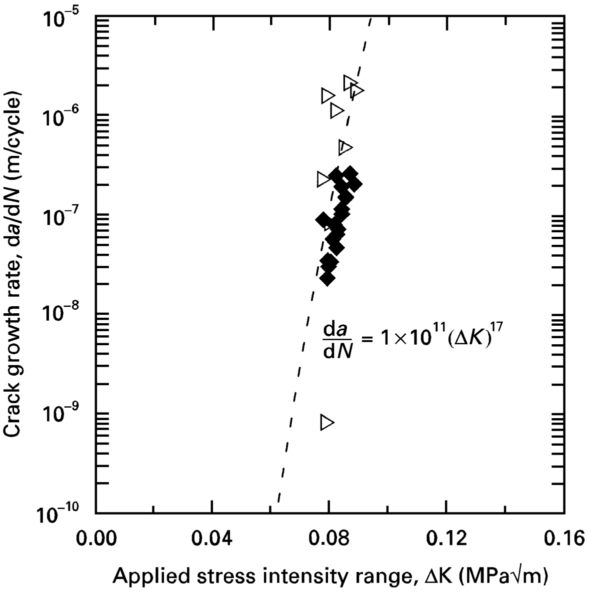

Figure 11 Experimental data showing cyclic fatigue-crack propagation rates, da/dN, as a function of the stress-intensity range, K ($= 0.9\, K_{max}$), for round disc-shaped compact tension DC(T) specimens of Norian SRS carbonated apatite containing long through-thickness cracks. Tests were performed in an environmental chamber containing de-ionized water. 25 Hz, R = 0.1. ◆ Test 1; ▷ Test 5.

In the fatigue of brittle materials like ceramics, considerable effort has recently been directed to demonstrating that fatigue crack growth is a true cyclic fatigue phenomena, and not simply associated with environmentally assisted crack growth [21, 22]. While a detailed description of the micromechanisms of fatigue crack growth in these materials remains elusive, it is now widely recognized that mechanisms acting *behind* the crack tip, such as progressive wear degradation of bridging grains and intact matrix elements in the crack wake, lead to a reduction of the associated toughening mechanism and exposure of the crack tip to more of the applied loads [22, 39, 41, 42, 45]. The problem in brittle materials has been to postulate mechanisms of fatigue damage which do not depend on dislocation motion and associated plasticity as is typical observed in metallic materials. Similar considerations may be applied to brittle cellular materials

TABLE III Values of C and m (in Equation 1) and the threshold ΔK_{TH} for some ceramic materials

Material	K_c (MPa m$^{1/2}$)	C (m/cycle(MPa m$^{1/2}$)$^{-m}$)	m	ΔK_{TH} (MPa m$^{1/2}$)	Ref.
Norian SRS Carbonated apatite	0.14	1.03×10^{11}	17	0.085	Present study
Al_2O_3–SiC_w	4.5	1.12×10^{-17}	15	2.7	39
Alumina (99.95% pure)	5.1	5.5×10^{-56}	32	2.8	41
Mg-PSZ (low to peak toughness)	2.9–16.0	2×10^{-14}–1.7×10^{-48}	21–42	1.6–7.7	21
Silicon nitride (NTK)	5.8	4.4×10^{-53}	30	3.4	42
Graphite/pyrolytic C	~ 1.6	1.86×10^{-18}	19	~ 0.6	23
Phenolic cellular Foam (170 kg/m^3)	0.05–0.08	9.58×10^{8}	10.4	0.015–0.022	29, 43
Cortical bone	3.2–8.0	1.47×10^{-18}	4.4	2.5	44, 45

which will exhibit only very limited, if any, dislocation activity. As discussed above, inelastic constitutive behaviour in the present carbonated apatite material may be associated with microcracking and rotation of cell walls to the tensile axis. Under repetitive fatigue loading, accumulated damage in the form of a microcracked zone ahead of the crack tip, together with wear degradation of unbroken cell walls and contacting asperities behind the crack tip may both contribute to cyclic fatigue crack growth. In addition, crack growth may be accelerated by the presence of the physiological environment through processes of slow crack growth (stress-corrosion cracking in metals terminology).

Some indication of the prevailing fracture mechanisms are obtained from fractographic analysis of the resulting fracture surfaces. While little discernible difference is apparent between the fast fracture and cyclic fatigue crack-growth regions at low magnification, a clear boundary between the two regions is nevertheless clearly apparent in the SEM micrograph shown in Fig. 12. At higher magnification, cyclic fatigue fracture surfaces were noticeably more rough and were seen to exhibit more particulate wear debris compared to the fast fracture surface (Fig. 13). Increasingly tortuous crack paths and rougher fracture surfaces were observed at near-threshold growth rates. These observations are consistent with similar studies in Al_2O_4 [41], Al_2O_3–SiC_w composites [39] and in Si_3N_4 ceramics [42], all of which are prone to progressive wear degradation of bringing zones formed behind the crack tip during cyclic fatigue. Alternatively, comparisons of fracture and fatigue fracture surfaces in pyrolythic carbon composites show little difference [22].

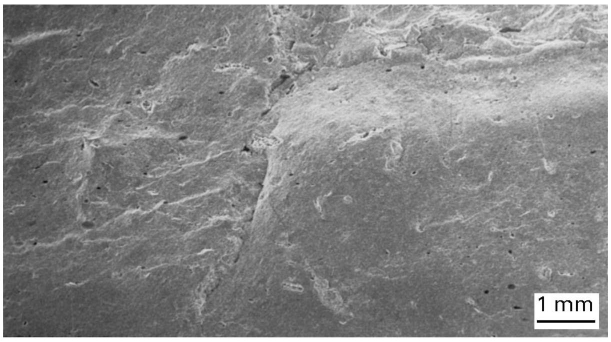

Figure 12 Low-magnification SEM micrograph of the fracture surface formed by fatigue and subsequently fast fracture. The boundary between the two regions is clearly apparent. Horizontal arrow indicates direction of crack growth.

Fatigue degradation has important consequences for the reliability and overall life of carbonated apatite materials used in structural applications involving repetitive loading. As discussed below, however, these may be significantly reduced by the progressive remodelling of these apatite materials. Similar to other safety-critical engineering components, fatigue life-prediction analyses can be based on continuum stress-life data obtained from smooth samples, or on a fracture mechanics defect tolerant approach [46]. There are three principal inputs to the more conservative defect tolerant approach: the initial flaw population or size of the largest (worst-case) crack pre-existing in the material (which must be delimited by quality and process controls), the critical flaw size for catastrophic failure (which in most cases is defined by the material's fracture toughness, K_c), and the rate at which the incipient cracks will grow subcritically between these two limits. Currently, for example, fatigue life analyses for pyrolytic-carbon/graphite heart valve implants utilize crack-propagation data conventionally measured on ASTM-style specimens with long, through-thickness cracks and from small, part-through (half-penny shaped) surface cracks [22, 23]. In order to guarantee adequate service life for these components, the initial defect sizes must be restricted to very small sizes due to the low fracture toughness and even lower stress intensities at which fatigue crack growth occurs.

Under this fatigue damage paradigm, it appears that similar stringent restrictions would be required for carbonated apatite materials. Both the extreme brittleness and high porosity of these materials make them inherently susceptible to premature brittle fracture. Modifications of the current processing route to reduce defect distributions together with toughening strategies possibly involving second-phase reinforcements are likely to produce significant enhancement of tensile strength, toughness and resistance to subcritical crack-growth. (Threshold stress intensity values for most brittle materials, unlike metals, are generally found to scale with the fracture toughness: ΔK_{TH} for fatigue crack growth in ceramics is typically ~ 50% K_{Ic} [39].) Importantly, however, it must be realized

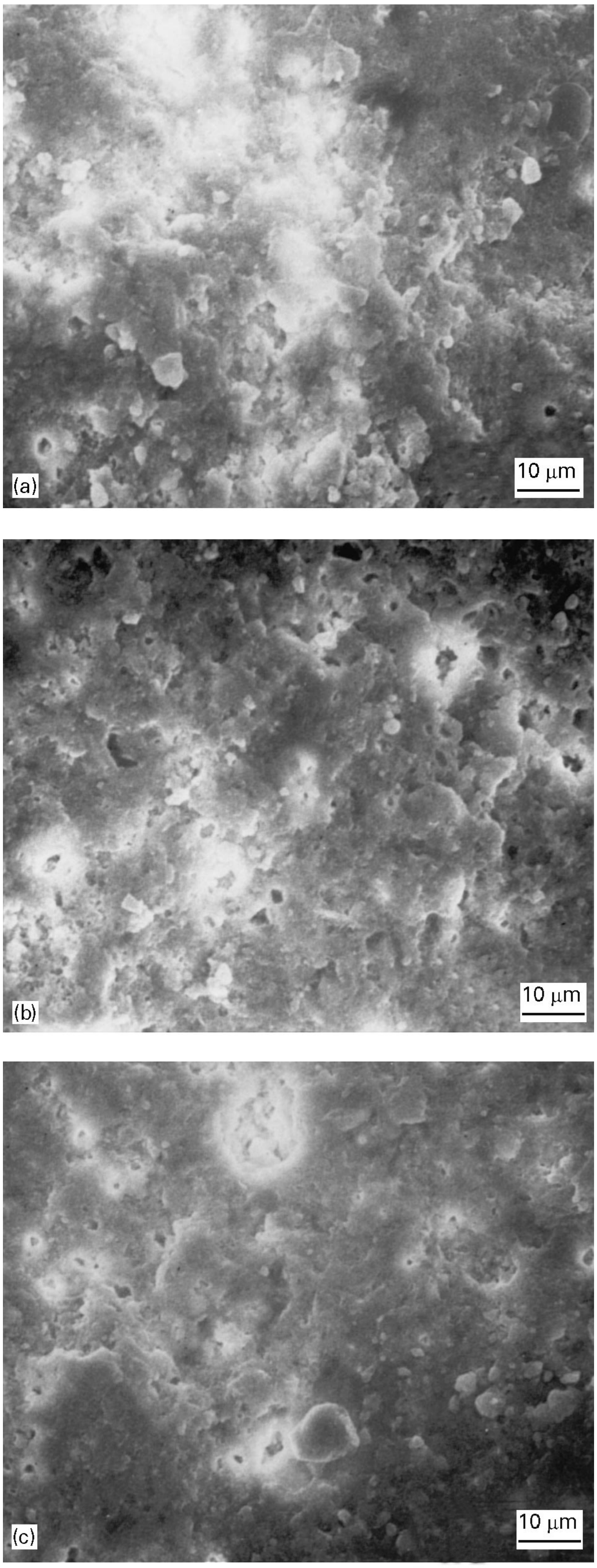

Figure 13 Higher magnification SEM micrographs showing (a, b) the increasingly rough fracture surfaces formed under decreasing cyclic fatigue crack-growth rates compared to (c) the smoother fast fracture surface. Evidence of particulate wear debris in clearly apparent on the fatigue fracture surfaces. Horizontal arrow indicates direction of crack growth.

that the effects of progressive remodelling that eventually leads to the replacement of the carbonated apatite material with new bone must be recognized in a more complete fatigue analysis. These effects are not currently included in typical fatigue life prediction methodologies used for biomedical devices. Two competing rate-dependent processes will therefore dictate the total life: the cycle-dependent fatigue damage mechanism, and the time-dependent remodelling process. Both of these processes depend on time, physiological loading cycles and stress levels. A full solution to this coupled rate-dependent process awaits further study.

4. Conclusions

The mechanical properties of a commercially available carbonated apatite, Norian SRS, formed at physiological temperature have been investigated. The following specific conclusions can be made:

1. Similar to the mineral phase of bone, the carbonated apatite material has a cellular microstructure which, from a mechanical property viewpoint, behaves like a brittle foam.
2. When formed at physiological temperature, carbonated apatite has a relatively high porosity ($\sim$ 50%) which contributes to a low flexural strength of $\sim$ 1.06 MPa in tension, compared to significantly higher reported compressive strength properties.
3. The brittle cellular foam structure of the carbonated apatite results in increasing measured hardness with decreasing indenter contact area.
4. Fracture toughness values were determined using both chevron notch and disc-shaped compact tension fracture mechanics samples containing atomically sharp pre-cracks. Low values of toughness of 0.06 MPa$\sqrt{m}$ and 0.14 MPa$\sqrt{m}$ were measured using the two techniques, respectively. Values are comparable with other brittle materials like chalk, dental enamel, sintered HA, brittle foams and dried bone tested at high strain rates.
5. Cyclic fatigue crack-growth rates, $\mathrm{d}a/\mathrm{d}N$, measured in de-ionized water were found to exhibit a power-law dependence on the applied stress intensity range, ΔK, similar to that commonly reported for a wide range of brittle ceramic materials with a crack growth exponent $m = 17$. A fatigue threshold value, ΔK_{TH}, defined for growth rates approaching $\sim 10^{-9}$ m/cycle, was found to be $\sim$ 0.085 MPa$\sqrt{m}$ or approximately 60% of the fracture toughness value K_{Ic}. Only brittle phenolic foams have reported fatigue crack-growth behavior at such low values of applied ΔK.
6. The low strength and toughness properties of carbonated apatite measured in tension are not necessarily inconsistent with the excellent performance of Norian SRS reported thus far in clinical trials where loading is principally in compression. When completely encased by bone, surrounding tendon and muscle tissue may be expected to create a compressive pre-load. In addition, the effect of constraint imposed by the adjacent bone substrates on the carbonated apatite in actual fixation applications may impart significant improvements in strength and reliability. These issues should be addressed in future studies.

Acknowledgements

The authors gratefully acknowledge the support of the Dana Adams Griffin Award received by RHD from the McCutchen Foundation, and experimental assistance from C. Nguyen and K. L. Ohashi, Department of Materials Science and Engineering, Stanford University.

References

1. P. M. BILLS and E. J. WHEELER, *J. Ed. Mod. for Mater. Sci. Engng.* **4** (1982) 391.
2. P. D. COSTANTINO, C. D. FRIEDMAN, K. JONES, L. C. CHOW, H. J. PELZER and G. A. SISSON, *Arch. Otolaryngol Head Neck Surg.* **117** (1991) 379.
3. H. OHGUSHI, M. OKUMURA, T. YOSHIKAWA, K. INOUE, N. SENPUKU and S. TAMAI, *J. Biomed. Mater. Res.* **26** (1992) 885.
4. I. C. ISON, M. T. FULMER, B. M. BARR and B. R. CONSTANTZ, in "Hydroxyapatite and related materials", edited by P. W. Brown and B. Constantz (CRC Press, 1994) p. 215.
5. G. VAES, *Clin. Orthopaed. Rel. Res.* **231** (1988) 239.
6. H. C. BLAIR, S. L. TEIDELBAUM, H. L. TAN, C. M. KOZIOL and P. H. SCHLESINGER, "Passive chloride permeability charge coupled to H^+-ATPase of Avian osteoclast ruffled membrane" *Am. J. Phys.* (1991) 260[6] C1315–1324.
7. Norian Corporation, "Chemical and crystallographic characteristics" (Mountain View, CA, 1994).
8. B. R. CONSTANTZ, I. C. ISON, M. T. FULMER, R. D. POSER, S. T. SMITH, M. VanWAGONER, J. ROSS, S. A. GOLDSTEIN, J. B. JUPITER and D. L. ROSENTHAL, *Science* **267** (1995) 1796.
9. M. VIGNOLES, G. BONEL, D. W. HOLCOMB and R. A. YOUNG, *Calcif. Tiss. Int.* **43** (1988) 33.
10. J. E. HARRIES, S. S. HASNAIN and J. S. SHAH, *ibid.* **41** (1987) 346.
11. R. M. BILTZ and E. D. PELLEGRNO, *Clin. Orth. Rel. Res.* **129** (1977) 279.
12. R. I. MARTIN and P. W. BROWN, *J. Mater. Sci. Mater. Med.* **6** (1995) 138.
13. P. VAN LANDUYT, F. LI, J. P. KEUSTERMANS, J. M. STREYIO, F. DELANNAY and E. MUNTING, *J. Mater. Sci. Mater. Med.* **6** (1995) 8.
14. H. AOKI, in "Science and medical applications of hydroxyapatite" (Takayama Press, 1991).
15. G. de WITH, H. J. A. van DIJK, N. HATTU and K. PRIJS, *J. Mater. Sci.* **16** (1981) 1592.
16. Norian Corporation, "The materials science of Norian SRS^{TM}, skeletal repair system" (Mountain View, CA, 1994)
17. F. I. BARATTA, W. T. MATHEWS and G. D. QUINN, "Errors associated with flexture testing of brittle materials" (US Army Materials Testing Laboratory, 1987).
18. D. G. MUNZ, J. L. SHANNON and R. T. BUBSEY, *Int. J. Fracture* **16** (1980) R137.
19. T. T. SHIH, *J. Test. Eval.* **9** (1981) 50.
20. G. HIMSOLT, D. MUNZ and T. FETT, Commun, *J. Amer. Ceram. Soc.* **70** (1987) C-133.
21. R. H. DAUSKARDT, D. B. MARSHAL and R. O. RITCHIE, *ibid.* **73** (1990) 893.
22. R. O. RITCHIE, R. H. DAUSKARDT, W. YU and A. M. BRENDZEL, *J. Biomed. Mater. Res.* **24** (1990) 189.
23. R. H. DAUSKARDT, R. O. RITCHIE, J. K. TAKEMOTO and A. M. BRENDZEL, *J. Biomech. Mater. Res.* **28** (1994) 791.
24. ASTM Standard E399-90, in "1990 ASTM annual book of standards", Vol 3.01. (American Society for Testing and Materials, Philadelphia, PA, 1990) p. 485.
25. J. E. SRAWLEY, *Int. J. Fracture* **12** (1976) 475.
26. M. D. DRORY, R. H. DAUSKARDT, A. KANT and R. O. RITCHIE, *J. Appl. Phys.* **78** (1995) 3083.
27. ASTM Standard E. 645-86a, in "1987 ASTM annual book of standards", Vol 3.01. (American Society for Testing and Materials, Philadelphia, PA, 1987) p. 899.
28. S. SURESH and R. O. RITCHIE, in "Fatigue crack growth threshold concepts", edited by D. L. Davidson and S. Suresh (The Metallurgical Society of the American Institute of Mining, Metallurgical, and Petroleum Engineers, Warrendale, PA, 1984) p. 227.
29. A. SAXENA, S. J. HUDAK, Jr., J. K. DONALD and D. W. SCHMIDT, *J. Test. Eval.* **6** (1978) 167.
30. Norian Corporation, "Mechanical and physical characteristics of Norian SRS skeletal repair system" (Mountain View, CA 1994).
31. L. J. GIBSON and M. F. ASHBY, in "Cellular solids: structure and properties" (Pergamon Press, New York, 1988) p. 316.
32. A. G. EVANS, *J. Amer. Ceram. Soc.* **73** (1990) 187.
33. R. H. DAUSKARDT and R. O. RITCHIE, in "An introduction to bioceramics", edited by L. L. Hench and J. Wilson (World Scientific, Singapore, 1993) p. 261.
34. R. HASSAN, A. A. CAPUTO and R. F. BUNSHAH, *J. Dent. Res.* **60** (1981) 820.
35. S. K. MAITI, M. F. ASHBY and L. J. GIBSON, *Sripta Metall.* **18** (1984) 213.
36. A. McLNTYRE and G. E. ANDERTON, *Polymer* **20** (1979) 247.
37. J. W. MELVIN, *J. Biomech. Eng., Trans. ASME* **115** (1993) 549.
38. W. BONFIELD and P. K. DATTA, *J. Mater. Sci.* **9** (1974) 1609.
39. R. H. DAUSKARDT, M. R. JAMES, J. R. PORTER and R. O. RICHIE, *J. Amer. Ceram. Soc.* **75** (1992) 759.
40. P. C. PARIS and F. ERDOGAN, *J. Basic Eng., Trans. ASME* **85** (1963) 528.
41. C. J. GILBERT, R. N. PETRANY, R. O. RITCHIE, R. H. DAUSKARDT and R. W. STEINBRECH, *J. Mater. Sci.* **30** (1995) 643.
42. C. J. GILBERT, R. H. DAUSKARDT and R. O. RITCHIE, *J. Amer. Ceram. Soc.* **78** (1995) 2291.
43. N. A. FLECK, K. J. KANG and M. F. ASHBY, *Acta Metall. Mater.* **42** (1994) 365.
44. T. M. WRIGHT and W. C. HAYES, *J. Biomed. Mater. Res. Symn.* **10** (1976) 637.
45. R. H. DAUSKARDT, *Acta Metall. Mater.* **41** (1993) 2765.
46. R. H. DAUSKARDT, R. O. RITCHIE and B. N. COX, *Adv. Mater. Proc.* **7** (1993) 26.
47. J. W. MELVIN, *J. Biomech. Eng.* **115** (1993) 549.

Received 30 July
and accepted 18 September 1996